

Origin of spin-glass and exchange bias in $\text{La}_{1/3}\text{Sr}_{2/3}\text{FeO}_{3-\gamma}$ nanoparticles

R. B. da Silva, J. H. de Araújo, J. M. Soares, and F. L. A. Machado

Citation: *Journal of Applied Physics* **115**, 113906 (2014); doi: 10.1063/1.4868685

View online: <https://doi.org/10.1063/1.4868685>

View Table of Contents: <http://aip.scitation.org/toc/jap/115/11>

Published by the [American Institute of Physics](#)

Articles you may be interested in

[Electronic phase diagram of epitaxial \$\text{La}_{1-x}\text{Sr}_x\text{FeO}_3\$ films](#)

Applied Physics Letters **105**, 062110 (2014); 10.1063/1.4893139

[Electronic transport and conduction mechanism transition in \$\text{La}_{1/3}\text{Sr}_{2/3}\text{FeO}_3\$ thin films](#)

Journal of Applied Physics **115**, 233704 (2014); 10.1063/1.4883541

[Exchange bias and memory effect in double perovskite \$\text{Sr}_2\text{FeCoO}_6\$](#)

Applied Physics Letters **101**, 142401 (2012); 10.1063/1.4756792

[Nature of short-range ferromagnetic ordered state above \$T_C\$ in double perovskite \$\text{La}_2\text{NiMnO}_6\$](#)

Applied Physics Letters **96**, 262507 (2010); 10.1063/1.3459141

[Charge order suppression and weak ferromagnetism in \$\text{La}_{1/3}\text{Sr}_{2/3}\text{FeO}_3\$ nanoparticles](#)

Applied Physics Letters **91**, 072504 (2007); 10.1063/1.2768895

Scilight

Sharp, quick summaries **illuminating**
the latest physics research

Sign up for **FREE!**

AIP
Publishing

Origin of spin-glass and exchange bias in $\text{La}_{1/3}\text{Sr}_{2/3}\text{FeO}_{3-\gamma}$ nanoparticles

R. B. da Silva,¹ J. H. de Araújo,¹ J. M. Soares,² and F. L. A. Machado³

¹Departamento de Física Teórica e Experimental, UFRN, Natal, Brazil

²Departamento de Física, UERN, Mossoró, RN, Brazil

³Departamento de Física, UFPE, Recife, PE, Brazil

(Received 28 August 2013; accepted 5 March 2014; published online 18 March 2014)

The structure and the magnetic properties of nanopowdered samples of $\text{La}_{1/3}\text{Sr}_{2/3}\text{FeO}_{3-\gamma}$ with average particles size d in the range of 67–367 nm prepared by a sol-gel method were investigated in detail. The samples were characterized by X-ray diffraction, scanning electron microscopy, specific heat, Mössbauer spectroscopy, ac susceptibility, and magnetization measurements. Exchange bias with vertical magnetization shift was found in all samples. Charge ordering and antiferromagnetism were observed close to 200 K for large particles ($d \geq 304$ nm) samples, while for particles with intermediated and smaller values ($d \leq 156$ nm) a cluster-glass like behaviour and a short range charge ordering were seen near 115 K and 200 K, respectively. The spin-glass like and exchange bias behaviour in nanopowdered samples of $\text{La}_{1/3}\text{Sr}_{2/3}\text{FeO}_{3-\gamma}$ are associated to compact Fe^{3+} antiferromagnetic (AF) clusters caused by an oxygen deficiency, which was found to be higher in the samples with the smallest average particles sizes. The effect of exchange bias and vertical magnetization shifts are explained by a simple model involving the interaction of one AF phase with a canted AF phase. © 2014 AIP Publishing LLC. [<http://dx.doi.org/10.1063/1.4868685>]

I. INTRODUCTION

The perovskite oxide system $\text{La}_{1-x}\text{Sr}_x\text{FeO}_{3-\gamma}$ (LSFO) ($0 \leq x \leq 1$) has attracted great scientific^{1–6} and technological attentions.^{7–12} They can be used, for instance, in fuel cells technologies and in gas sensors. Their physical properties are strongly influenced by their chemical composition and by their crystalline structures. For instance, LaFeO_3 (LFO) exhibits an orthorhombical structure with space group Pbnm and it is an antiferromagnetic (AF) insulator with a Néel temperature T_N of approximately 750 K.¹³ The structure of SrFeO_3 (SFO), on the other hand, is cubic with a space group Pm-3m and it is a metallic AF with a T_N of 134 K.¹⁴ Thus, by replacing La^{3+} by Sr^{2+} one observes an increase in the electronic conduction and a reduction in T_N .¹⁵ The ionic substitution increases the valence state of Fe ion from 3+ (LFO) to 4+ (SFO). For low Sr concentrations ($0 \leq x \leq 0.3$), magnetic measurements indicated the existence of weak ferromagnetism with the spontaneous magnetization decreasing with increasing Sr content.¹⁶ At intermediate Sr concentration, a sequence of Fe^{3+} and Fe^{4+} observed at low temperature has been explained on the basis of the local charge ordering (CO) state.¹⁷ Besides, for concentrations close to 2/3 a charge ordering has been observed with a Verwey transition temperature T_V of about 210 K.⁵ Charge disproportion occurs on the Fe sites, from an average valence state $\text{Fe}^{3.67+}$ in the paramagnetic phase into a mixture of $2\text{Fe}^{3+} + 1\text{Fe}^{5+}$ in the antiferromagnetic CO state below 210 K.^{18,19} Moreover, the antiferromagnetic (J_{AF}) and ferromagnetic (J_F) superexchange interactions between the pairs $\text{Fe}^{3+}\text{-Fe}^{3+}$ and $\text{Fe}^{3+}\text{-Fe}^{5+}$, respectively, were found to be consistent with both charge and spin ordered structures.²⁰ Inelastic neutron scattering has been used to determine the values of J_F and J_{AF} . The measured exchange ratio J_F/J_{AF} ($|J_F/J_{AF}| > 1$) was found to fulfill the criterion for CO driven by magnetic interactions.²¹

Despite the extensive literature and well elaborated studies in bulk materials, some open questions in nanoparticles demand for more theoretical and experimental work. For example, polycrystalline samples of $\text{La}_{1/3}\text{Sr}_{2/3}\text{FeO}_{3-\gamma}$ with average particle size in the range of 80–2000 nm have been studied by magnetization and specific heat measurements.²² The authors have argued that the charge ordering state could be suppressed by reducing the particle size. Moreover, the high coercivity hysteresis behavior observed at room temperature in the samples with diameter less than 300 nm was interpreted by weak ferromagnetism attributed to the lattice distortion.

Recently, Sabyasachi *et al.*²³ have studied bulk and nanocrystalline LSFO with this same sample concentration by using ac and dc magnetization, Mössbauer spectroscopy, and polarized neutron diffraction. At room temperature, the bulk sample is paramagnetic, while the nanocrystalline is not. An exchange-bias effect was observed in the nanocrystalline samples at 5 K, which was attributed to a phase separation caused by a destabilization of the charge ordering state. Moreover, the frequency dependence in the ac magnetic susceptibility below 65 K was interpreted as a cluster-glass (CG) state. Nevertheless, the origin of the spin glass behaviour and its relation to exchange bias (EB) are not very clear.

In this work, we synthesize high quality LSFO samples within a broad range of average particle size (67–367 nm) for $x=2/3$ by using a sol-gel method. The samples were characterized by X-ray diffraction (XRD), scanning electron microscopy (SEM), Mössbauer spectroscopy, specific heat, magnetization, and ac magnetic susceptibility measurements. All samples studied here are paramagnetic at room temperature and display exchange bias with vertical magnetization shift at 5 K. The nanoparticulated powder showed spin-glass behaviour and short-range charge ordering for intermediate

and small particle sizes, while for larger particle sizes anti-ferromagnetism and charge ordering are the dominating magnetic states. Moreover, we show that the effect of spin glass and exchange bias is related to oxygen deficiency. Finally, the room temperature high coercivity and the large magnetic moments values reported in Ref. 22 for particles with average size smaller than 300 nm were not observed in the samples investigated in the present work.

II. EXPERIMENTAL

$\text{La}_{1/3}\text{Sr}_{2/3}\text{FeO}_{3-\gamma}$ (LSFO) perovskites were prepared by using a sol-gel method. $\text{La}(\text{NO}_3)_3 \cdot 6\text{H}_2\text{O}$, $\text{Sr}(\text{NO}_3)_2$, $\text{Fe}(\text{NO}_3)_3 \cdot 9\text{H}_2\text{O}$, ethylene glycol, and citric acid monohydrate were used as the raw materials. Few steps are required for synthesizing the samples. First, 1M-aqueous solutions for each of the metal nitrates and for the citric acid were prepared. Next, appropriate volumes according to the atomic ratio of La, Sr, and Fe in $\text{La}_{1/3}\text{Sr}_{2/3}\text{FeO}_{3-\gamma}$ of the metal nitrate solutions were poured into a beaker and mixed. A volume of the citric acid solution similar to the mixture of metal nitrate solution was then added to the beaker and mixed for homogenizing the final solution. For instance, for producing 1 g of sample material a ratio of 1.02:0.09:1.05:1.66 cm^3 for the volumes of the lanthanum nitrate, strontium nitrate, iron nitrate, and citric acid solutions, respectively, is required. Subsequently, the solution was evaporated for about 4 h at 100 °C to form a gel. The gel was then crushed and decomposed at 400 °C for 2 h. Finally, it was divided in four parts and calcinated in air for 4 h at 900 °C, 1000 °C, 1100 °C, and 1200 °C. These samples will be referred from now on, respectively, as LSFO900, LSFO1000, LSFO1100, and LSFO1200.

Diffraction (XRD) patterns were obtained by using the Cu-K α radiation and by recording the data every 0.02° at a sweeping rate of 2°/min. The MAUD code^{24–26} and the Rietveld procedure were employed for refining the XRD data allowing the determination of the average size of the crystallites and of the crystalline structures. A scanning electron microscope Tescan-MIRA3 LMU was used for analyzing the microstructure of the samples. For these analyses, a droplet made of small amounts of the powder samples dispersed in ethanol was placed on carbon tapes. ⁵⁷Fe Mössbauer effect measurements were carried out at room temperature by using a constant acceleration spectrometer, operating in the triangular wave mode, and by using a ⁵⁷Co source in a rhodium matrix, in the conventional transmission geometry. The spectrometer was calibrated with a 25 μm thick α -Fe foil. The magnetization, the specific heat, and the ac magnetic susceptibility were measured by using a Physical Properties Measurement System—PPMS made by Quantum Design.

III. RESULTS AND DISCUSSION

XRD patterns for LSFO samples calcinated at different temperatures are shown in Fig. 1. All samples were found to be single phase within the resolution of the XRD technique. The diffraction peaks were refined using a perovskite-type rhombohedral structure with space group $R\bar{3}c$ in the trigonal system. The crystallite sizes obtained from the refinements were 67 nm, 156 nm, 304 nm, and 369 nm for the LSFO900, LSFO1000, LSFO1100, and LSFO1200, respectively. A slight contraction in the lattice parameters with increasing particle size was observed (see insets of Fig. 1). This behaviour has been interpreted as due to a deficiency in the

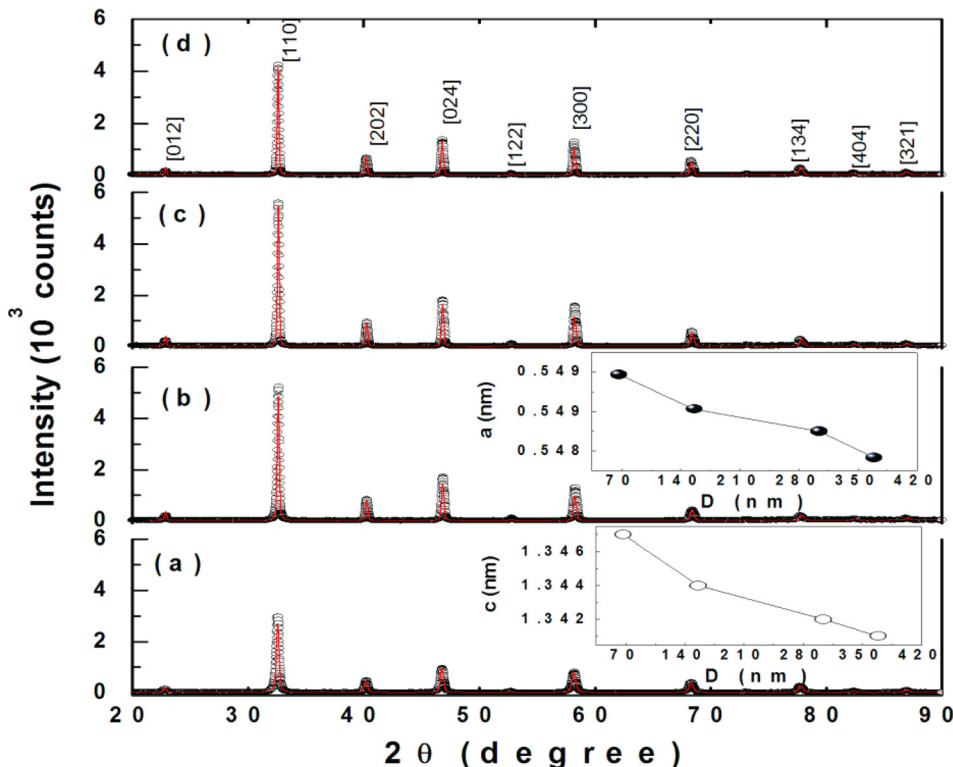


FIG. 1. XRD patterns for nanopowder samples of $\text{La}_{1/3}\text{Sr}_{2/3}\text{FeO}_{3-\gamma}$ calcinated at 900 °C (a), 1000 °C (b), 1100 °C (c), and 1200 °C (d). The inset shows the lattice parameters a and c as a function of the average particle size.

oxygen content, which becomes even more important in the samples with the smallest average particle sizes.^{27,28}

The morphology, the nanometric nature, and the particle size distribution of the calcined samples were investigated by SEM and the results are shown in Fig. 2. Despite the fact that the particle size distributions are relatively wide, the average particle size was found to vary substantially with the calcination temperature. The morphology of the particles was found to be homogeneous despite the large particle size variation produced by the sol-gel technique and by the calcination temperature. Moreover, the average particle sizes observed by the SEM micrographs are in good agreement with those obtained by XRD.

The main part of Fig. 3 shows hysteresis loops for the calcined samples obtained after cooling the samples from room temperature down to 5 K at an applied magnetic field of 50 kOe. It is interesting to notice the presence of horizontal and vertical shifts in the hysteresis loops induced by the cooling field. Asymmetric shifts have been observed in dilute alloys,²⁹ thin films,³⁰ and structured nanoparticles.³¹ In the present work, we have adopted the more currently used name, i.e., exchange-bias effect, to refer to the shift along the magnetic field axis. Moreover, the values for the corresponding exchange-bias field and vertical magnetization shift were found to increase with decreasing values of the average particle size (see Fig. 3(b)). The order of magnitude of the exchange-bias fields is also close to the ones observed by Sabyasachi *et al.*²³ However, the coercivities measured by those authors are substantially larger than the ones reported here. Besides, the high coercivities at room temperature reported in Ref. 22 were not observed in the samples used in the present work. Indeed, the samples used in the present work were found to be paramagnetic at room temperature as expected for this sample composition ($x = 2/3$) and shown

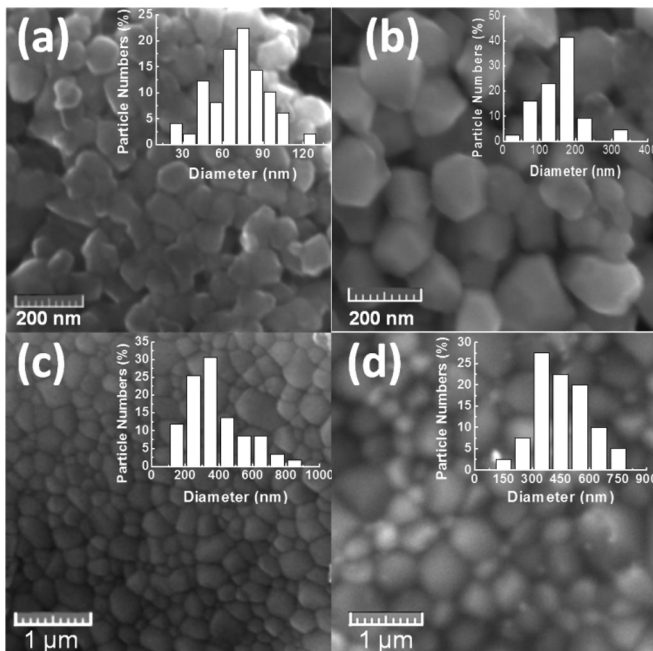


FIG. 2. SEM images for nanopowder samples of $\text{La}_{1/3}\text{Sr}_{2/3}\text{FeO}_{3-\gamma}$ calcined at 900°C (a), 1000°C (b), 1100°C (c), and 1200°C (d). The insets are the corresponding particle size histograms.

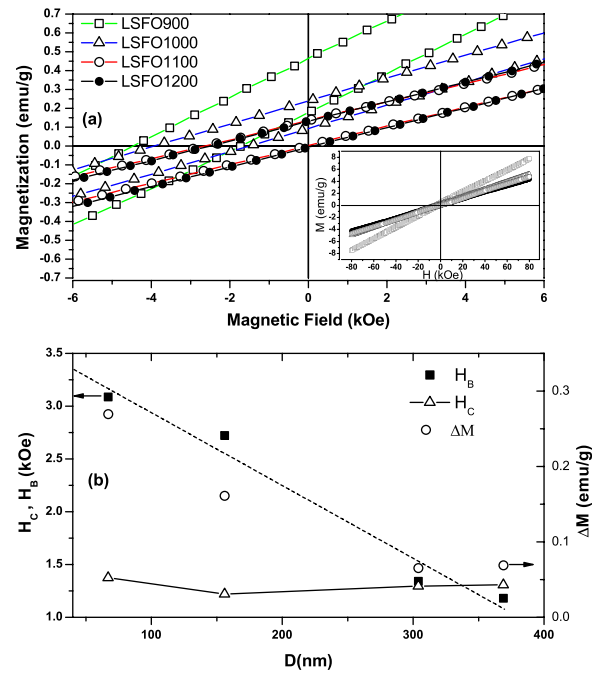


FIG. 3. Magnetic hysteresis loop for the calcined samples of LSFO measured at 5 K after cooling the samples at a magnetic field of 50 kOe (a). The inset of Fig. 3(a) shows a zoom around origin. The dependence of the coercive field H_c (open triangles), exchange-bias field H_B (closed square), and the magnetization shift (open circles) with the average size of the nanoparticles is shown in (b). The lines are guide to the eyes.

by the hysteresis loops in Fig. 4. We can see from Fig. 4 that at room temperature the magnetization increases with the calcination temperature. This behavior is due to the fact that the ratio of $\text{Fe}^{4+}/\text{Fe}^{3+}$ does also increase with the calcination temperature, leading to a higher magnetization at the highest applied field. Hysteresis loops measured at 5 K under zero field cooled (ZFC) are shown in the inset of Fig. 4, where we can see behaviors symmetric around the origin due to the existence of weak ferromagnetism. Remanent magnetization was also found to increase with the calcination temperature. This behavior is consistent with the fact that the spin-canting is higher in samples calcinated at higher temperatures.

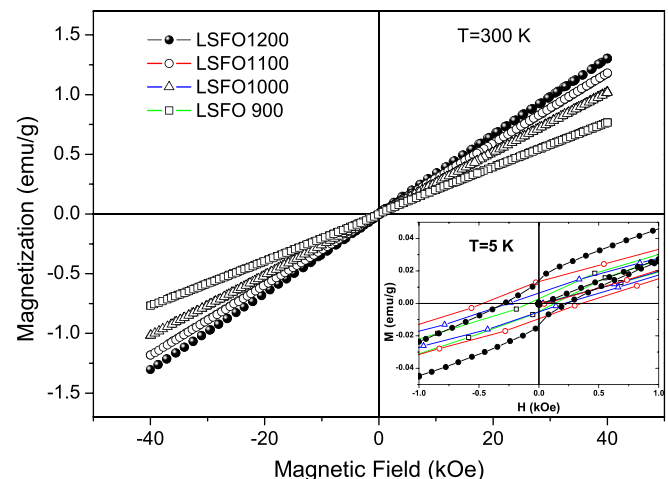


FIG. 4. Magnetic hysteresis loop for the calcined samples of LSFO measured at room temperature. The inset are hysteresis loops measured at 5 K after cooling the sample with no applied field.

The temperature dependence for the ZFC and field cooled (FC) magnetizations is shown in Fig. 5. For samples LSFO1100 and LSFO1200, the ZFC magnetization curves decrease with increasing temperature reaching a minimum at around 170 K, after shows an abrupt increasing with a peak around 200 K. After this temperature, the curves decrease linearly with the temperature, in good agreement with the measurements obtained by other groups.^{5,27} This behavior could be attributed to charge ordering transition and antiferromagnetic ordering temperatures T_{CO} and T_N , which are both close to 200 K for these samples.

The other samples, LSFO900 and LSFO1000, show more complex magnetization curves. In a scale almost three times smaller, the curves increase with increasing temperature showing a little plateau around 120 K and further a peak around 200 K, but after this temperature, the curves decrease with the temperature non-linearly. A similar behavior, with a broad peak around 150 K, was observed by Wu *et al.*²⁷ in a sample with oxygen vacancy. Moreover, the ZFC and FC curves cross each other near 150 K.

The temperature dependence for the in-phase component of the ac magnetic susceptibility (χ') is shown in Fig. 6. The measurements were performed by keeping the magnitude of the ac magnetic field constant ($h_{ac} = 10$ Oe) and by setting the frequency (f) at 100 Hz, 1 kHz, and 10 kHz. While no significant effect is observed for the samples with large particles (LSFO1100 and LSFO1200), a bump which shifts towards high values of T with increasing values of f was observed for the other two samples (LSFO900 and LSFO1000). This behaviour is a signature of spin-glass like systems. The temperature dependence of the ac susceptibility of a cluster-glass is actually given by a somewhat broad cusp. Besides the cusp, a peak at T_N and T_{CO} near 200 K at

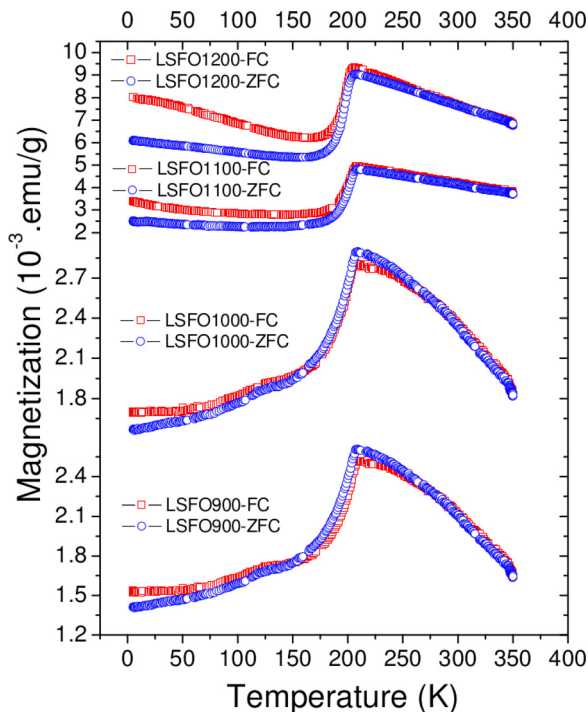


FIG. 5. Field-cooled (squares) and zero-field-cooled (circles) magnetizations for calcined samples of LSFO measured for $H = 100$ Oe.

the T-dependence of the dc magnetization for samples LSFO900 and LSFO1000 is also expected. However, the magnetization for these samples is significantly smaller than those for the other two samples (see Fig. 5). Moreover, the peaks at T_N and T_{CO} are close to the spin-glass-like transition temperature. So, the superposition of the cusp with the peak at T_N and T_{CO} yields the broader peaks observed in Figs. 6(a) and 6(b) in contrast to the sharper ones observed in Figs. 6(c) and 6(d). The f -dependence of χ' for samples LSFO900 and LSFO1000 was analyzed by using the critical slowing down model.³² Within this model, the relaxation time τ is given by

$$\tau = \tau_0 \left(\frac{T_f}{T_g} - 1 \right)^{-z\nu}, \quad (1)$$

where τ_0 is the characteristic time scale of the system, T_g is the spin glass transition, T_f is the temperature corresponding to the peak of χ' (freezing temperature), and z and ν are the critical exponents. The correlation time τ , determined by the reciprocal of the frequency of the driving ac field, was plotted against the reduced temperature $(\frac{T_f}{T_g} - 1)$ in a log-log plot for samples LSFO900 and LSFO1000. These results are shown in Fig. 6(e). The linearization of the data was obtained by using $T_g = 115.34$ K (114.71 K) in the calculation of the reduced temperature for LSFO900 (LSFO1000). The LSFO900 (LSFO1000) data was then fit by using Eq. (1) yielding $z\nu = 7.23 \pm 0.42$ (7.34 ± 0.45) and $\tau_0 = (2.18 \pm 0.32 \times 10^{-7})$ s ($(2.22 \pm 0.34) \times 10^{-7}$ s). The values for $z\nu$ for these two samples are in the range typically found for spin glass systems ($z\nu \sim 6 - 12$). However, the values of τ_0 are few order of magnitude larger than those obtained for canonical spin-glass ($\tau_0 \sim 10^{-13}$),³³ although they are in good agreement with the ones obtained for CG systems ($\tau \sim 10^{-7} - 10^{-9}$).^{34,35}

The overall results obtained through the magnetization and ac magnetic susceptibility measurements are also consistent with specific heat (c_p) data obtained for the calcined samples (Fig. 7). First, a large thermal hysteresis was observed for the two samples with larger average particle sizes (LSFO1100 and LSFO1200). This behaviour is typical of first-order phase transitions and it is expected near the CO transition temperature ($T_{CO} \sim 200$ K). For LSFO900 and LSFO1000, a bump in c_p not seen in the other two samples is observed at lower temperatures, while the peak near 200 K for the first one seems to vanish. The bump plus the f -dependence of χ'_{ac} are signature of spin-glass systems. The spin-glass-like behavior plus a contribution to the Mössbauer spectrum (shown later in the paper) due to conversion of Fe^{5+} into Fe^{3+} are clear indications that the long range correlation formed by the $Fe^{3+}-Fe^{5+}$ is not completed yet in LSFO900 and LSFO1000. This, in turn, is also consistent with the broadening and reduction of the peak near T_{CO}/T_N .

It is worth to reminder that these are the samples that presented a significant frequency dependence in χ' . Because of the somewhat large particle size distribution, a residual peak due to the long range order is still seen in the c_p data for the sample LSFO1000 but it is completely absent for sample LSFO9000.

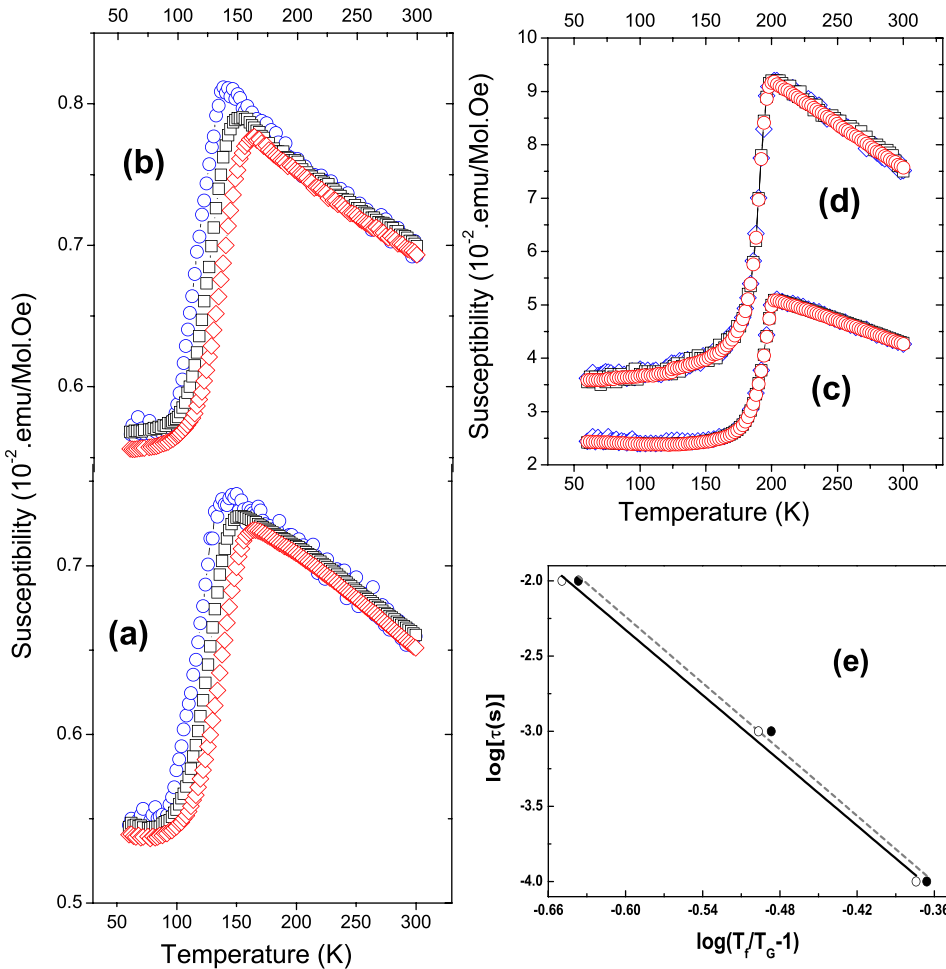


FIG. 6. In-phase component of the ac magnetic susceptibility measured for $h_{ac} = 10$ Oe and $f = 100$ Hz (open circles), 1 kHz (open squares) and 10 kHz (open diamonds) for samples calcined at 900°C (a), 1000°C (b), 1100°C (c), and 1200°C (d). A log-log plot of the relaxation time vs. reduced temperature is shown in (e) for samples LSFO900 (open circles) and LSFO1000 (closed circles). The solid and dashed lines are fit to a theoretical model.

A mechanism which is being attributed as responsible for decreasing the magnetization and for establishing an onset for a glassy phase at low temperatures is the oxygen

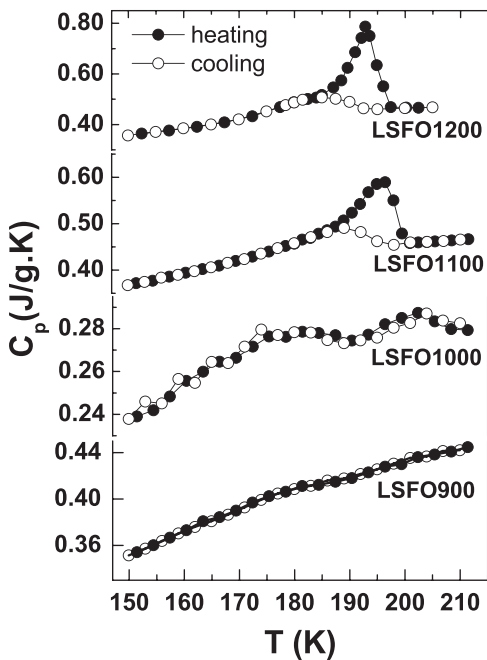


FIG. 7. Specific heat data measured while heating up (•) and cooling down (◦) the samples.

deficiency. This mechanism is also expected to be more important for the samples with smaller particle size. By decreasing the oxygen content one would expect an increase in the amount of Fe^{3+} with a correspondent decreasing in the amount of Fe^{4+} . This effect unbalances the amount of ferromagnetic $Fe^{3+}-Fe^{5+}$ (J_F) and antiferromagnetic $Fe^{3+}-Fe^{3+}$ (J_{AF}) bonds leaving the non-homogeneous distribution which, in turn, leads to spin-glass like behavior. An unbalancing in the nature of the bounds may also be obtained in the absence of oxygen deficiency. For instance, spin glass behavior was also observed in bulk samples of $La_{1-x}Sr_xFeO_{3-\gamma}$ with $x = 0.5, 0.55, \text{ and } 0.6$, at temperatures around 160 K. However, in this set of samples the increasing in the Fe^{3+} content is mainly due to the fact that the samples have smaller concentration of their compositions.³⁶

The scenario pictured above can be readily verified by Mössbauer spectroscopy. For instance, the spectra recorded at 300 K for the calcined samples are shown in Figs. 8(a) (LSFO1200), 8(b) (LSFO1100), 8(c) (LSFO1000), and 8(d) (LSFO900). We were able to fit (solid lines) the spectra by using two doublet curves, which are characteristics of paramagnetic states. The doublet with lower isomer shift δ was assigned to the Fe^{4+} ions, while the higher isomer shift was assigned to the Fe^{3+} following previously reported results.^{2,37} The parameters used for fitting the spectra are listed in Table I. It is important to stress that the area A under the Fe^{3+} doublet curve is larger for the samples with smaller

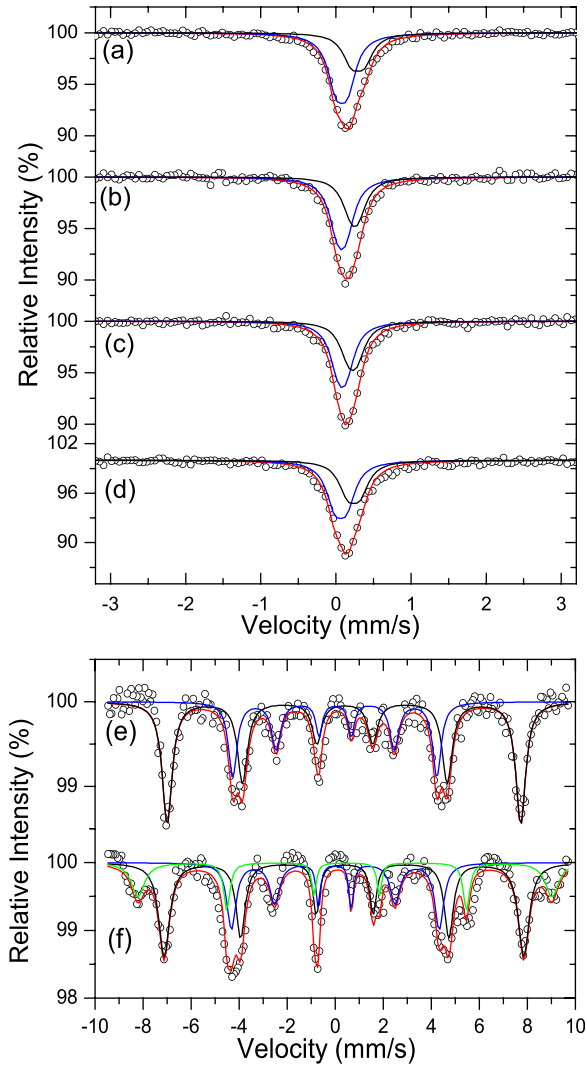


FIG. 8. Mössbauer spectra recorded at room temperature for samples LSFO1200 (a), LSFO1100 (b), LSFO1000 (c), and LSFO900 (d), and at 10 K for samples LSFO1200 (e) and LSFO900 (f). The lines are doublet and sextet components used for fitting the data.

particle size. Moreover, the ratio of the doublet areas $\text{Fe}^{3+}/\text{Fe}^{4+}$ is 0.76 for LSFO900, while its value is 0.57 for LSFO1200. The data listed in Table I were used for determining the ratio $\text{Fe}^{3+}/\text{Fe}^{4+}$ yielding the corresponding oxygen deficiencies γ ($=0.170$ for LSFO900, 0.0138 for LSFO1000, 0.120 for LSFO1100, and 0.056 for LSFO1200).

The Mössbauer spectra were also recorded at 10 K for the samples with the largest (LSFO1200) and the smallest

TABLE I. Mössbauer parameters for LSFO samples at room temperature.

Sample	Site	δ (mm/s)	ΔE_Q (mm/s)	A (%)
LSFO900	Fe^{4+}	0.064	0.156	56.9
	Fe^{3+}	0.238	0.163	43.1
LSFO1000	Fe^{4+}	0.085	0.105	58.9
	Fe^{3+}	0.227	0.109	41.1
LSFO1100	Fe^{4+}	0.077	0.102	59.9
	Fe^{3+}	0.249	0.115	40.1
LSFO1200	Fe^{4+}	0.079	0.151	63.6
	Fe^{3+}	0.291	0.168	36.4

(LSFO900) particle sizes. These results are shown in Figs. 8(e) and 8(f). It was found that the spectrum for the LSFO1200 samples could be fitted by using two sextets only. The sextet with larger isomer shift ($\delta = 0.382$ mm/s) was assigned to the Fe^{3+} ions, while the one with negative and smaller isomer shift ($\delta = -0.015$ mm/s) to the Fe^{5+} ions. Note that this spectrum is similar to the Mössbauer spectrum of the nanoparticulate sample of Sabyasachi *et al.*²³ However, in order to make a good fit in the spectrum for the LSFO900 sample, a third sextet with higher hyperfine field and higher isomer shift has to be assigned to Fe^{3+} following the procedure used by other research groups for these sample materials.^{5,37} The fitting parameters for the spectra recorded at 10 K are listed in Table II. The value of the H_{hf} ($=53.56$ T) for the Fe^{3+} yielded by fitting of the additional sextet in LSFO900 is significantly higher than the one for the Fe^{3+} ions in LSFO1200. However, values of H_{hf} for Fe^{3+} were also found in the range of 54–56 T for bulk samples of $\text{La}_{0.6}\text{Sr}_{0.4}\text{FeO}_3$ and LaFeO_3 .^{5,37} In the particles model discussed below, it is believed that the LSFO900 sample is composed by two types of magnetic clusters. The first one is a soft phase where the ferromagnetic interactions $\text{Fe}^{3+}-\text{Fe}^{5+}$ dominate, while the second phase is a hard antiferromagnet in character with predominant $\text{Fe}^{3+}-\text{Fe}^{3+}$ interactions yielding the large value for H_{hf} . We believe that the competition among these two phases leads to the spin-glass phase and to the exchange-bias effect reported above.

The value of A determined by the sextets used for fitting the Mössbauer spectra at 10 K allows one to estimate the ratio of the amount of Fe^{3+} and Fe^{5+} ions present in the samples. For instance, by taking the ratio of the areas given in Table II for sample LSFO1200 one gets 1.88. This is a value close to 2, which is the value required for the ratio of $\text{Fe}^{3+}/\text{Fe}^{5+}$ for a full charge ordering to take place. However, the ratio $\text{Fe}^{3+}/\text{Fe}^{5+}$ for the LSFO900 sample is 2.44. This value is substantially higher than 2 and it indicates that the long range CO cannot be established leading to a short range charge ordering regime distinct of the Fe^{3+} and Fe^{4+} local CO state.¹⁷ Indeed, it is expected the increase in the amount of Fe^{3+} caused by oxygen deficiency to interrupt the long-range sequence of $\text{Fe}^{3+}\text{Fe}^{3+}\text{Fe}^{5+}\text{Fe}^{3+}\text{Fe}^{3+}\text{Fe}^{5+}$ allowing the formation of compact Fe^{3+} AF clusters, with higher hyperfine field. These AF clusters are magnetically similar to an independent local phase. Since they have a stronger hyperfine field, their exchange interactions are also stronger, affecting the magnetic behavior in their neighborhood.

The magnetic behaviour in this system involves exchange coupling between a “soft” AF phase (with Fe^{3+} and Fe^{5+}) carrying a net moment due to spin imbalance and

TABLE II. Mössbauer parameters measured at 10 K.

Sample	Site	H_{hf} (T)	δ (mm/s)	ε_Q (mm/s)	A (%)
LSFO1200	Fe^{3+}	45.75	0.382	0.036	65.3
	Fe^{5+}	26.41	-0.015	0.015	34.7
LSFO900	Fe^{3+}	45.53	0.379	0.032	49.1
	Fe^{5+}	26.80	-0.005	0.021	29.1
	Fe^{3+}	53.56	0.439	0.072	21.8

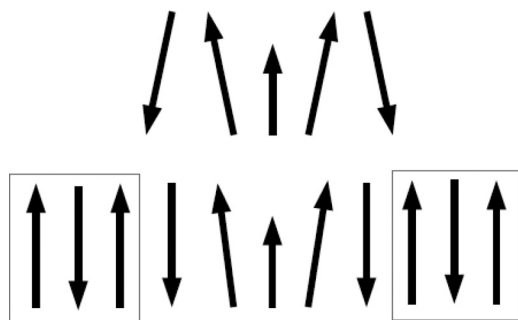


FIG. 9. Schematic diagrams of the magnetic configuration.

a “hard” AF phase (with only Fe^{3+}). Fig. 9 shows a schematic representation, based on Refs. 17 and 20, of a simplified (one-dimensional) magnetic configuration proposed to phenomenologically explain the magnetic behaviour in our samples. At the top of Fig. 9 is shown the representation of the “soft” AF phase, where we can see a small canting of the spins in the AF bonds. When the “soft” phase is dominant, it is observed long-range CO as in the samples LSFO1100 and LSFO1200. Particularly in the LSFO1200 sample, where the presence of the hard phase is very small, weak ferromagnetism is too observed (inset of Fig. 4).

The increase of “hard” phase caused by oxygen deficiency in the smaller particles interrupts the long-range CO state so that the “soft” phase remains in isolated clusters, allowing for the development of cluster-glass behaviour.

Magnetic EB is a phenomenon whereby the hysteresis loop of a “soft” magnetic phase is shifted by an amount H_B along the applied field axis owing to its interaction with a “hard” magnetic phase. The interfaces between the hard and soft phases, commonly, are between an antiferromagnetic phase and a ferro- or ferrimagnetic phase.^{38,39} However, similar to the results presented here, EB also has been observed in systems with a canted AF phase acting as the “soft” magnetic phase, and a balanced AF phase acting as the “hard” magnetic phase.⁴⁰ Some local realignment of spins close to the interface is required to yield the observed EB behavior. Fe^{3+} ions belongs to soft phase at the interface with the hard phase pinned (bottom of Fig. 9), making it harder leading to EB and vertical magnetization shifts observed in our samples.

IV. CONCLUSIONS

The magnetic properties of high quality nanoparticulate samples of the $\text{La}_{1/3}\text{Sr}_{2/3}\text{FeO}_{3-\gamma}$ perovskite were investigated in detail by using magnetization, ac susceptibility, and specific heat measurements. Exchange bias with vertical magnetization shift was found in all samples. The samples with average particles sizes of 304 nm and 369 nm presented simultaneously long range charge ordering and antiferromagnetism below about 200 K. For the samples with average particle size of 67 nm and 156 nm, instead, the samples shown short range charge ordering and a spin-glass like phase with a T_g around 115 K. The f -dependent contribution of χ'_{ac} was found to be more significant in the temperature range of 100–200 K, plus the FC and ZFC behavior and the bump in

the c_p data, allowed us to conclude that in this range of temperature the behavior is similar to the one expected for spin-glass like phase. Moreover, the f -dependence of χ'_{ac} was also found to be consistent with the critical slowing down model yielding parameters that are in agreement with those expected for such systems. These results were interpreted as been due to compact Fe^{3+} clusters caused by oxygen deficiency in the sample composition which, in turn, unbalances the amount of the ferromagnetic and antiferromagnetic bonds. It is also more important in the samples with the smallest particle size. The presence of oxygen deficiency in nanopowder samples is in good agreement with the observations made by Mössbauer spectroscopy.

ACKNOWLEDGMENTS

This work was partially supported by the Brazilian agencies CNPq, FINEP, CAPES, and FACEPE.

- ¹D. Treves, M. Eibschutz, and P. Coppens, *Phys. Lett.* **18**, 216 (1965).
- ²U. Shimony and J. M. Knudsen, *Phys. Rev. B* **144**, 361 (1966).
- ³S. E. Dann, D. B. Currie, M. T. Weller, M. F. Thomas, and A. D. Al-Rawwas, *J. Solid State Chem.* **109**, 134 (1994).
- ⁴W. F. Kelly, M.S. thesis, Massachusetts Institute of Technology, 1961.
- ⁵M. Takano, J. Kawachi, N. Nakanishi, and Y. Takeda, *J. Solid State Chem.* **39**, 75 (1981).
- ⁶J. B. Yang, X. D. Zhou, Z. Chu, W. M. Hikal, Q. Cai, J. C. Ho, D. C. Kundaliya, W. B. Yelon, W. J. James, H. U. Anderson, H. H. Hamdeh, and S. K. Malik, *J. Phys.: Condens. Matter* **15**, 5093 (2003).
- ⁷M. W. Son, J. B. Choi, H. J. Kim, and K. S. Yoo, *J. Korean Phys. Soc.* **54**, 1072 (2009).
- ⁸K. Fan, H. Qin, L. Wang, L. Ju, and J. Hu, *Sens. Actuators, B* **177**, 265 (2013).
- ⁹V. L. Kozhevnikov, I. A. Leonidov, M. V. Patrakeev, A. A. Markov, and Y. N. Blinovskov, *J. Solid State Electrochem.* **13**, 391 (2009).
- ¹⁰D. Bayraktar, S. Diethelm, T. Graule, J. Van Herle, and P. Holtappels, *J. Electroceram.* **22**, 55 (2009).
- ¹¹P. Plonczak, M. Gazda, B. Kusz, and P. Jasinski, *J. Power Sources* **181**, 1 (2008).
- ¹²A. Evdou, V. Zaspalis, and L. Nalbandian, *Fuel* **89**, 1265 (2010).
- ¹³M. Esbschütz, S. Shtrikman, and D. Trevis, *Phys. Rev.* **156**, 562 (1967).
- ¹⁴J. B. MacChesney, R. C. Sherwood, and J. F. Potter, *J. Phys. Chem.* **43**, 1907 (1965).
- ¹⁵A. Wattiaux, J. C. Grenier, M. Pouchard, and P. Hagenmuller, *J. Electrochem. Soc.* **134**, 1718 (1987).
- ¹⁶J. Li, X. Kou, Y. Qin, and H. He, *Phys. Status Solidi A* **191**, 255 (2002).
- ¹⁷J. Q. Li, Y. Matsui, S. K. Park, and Y. Tokura, *Phys. Rev. Lett.* **79**, 297 (1997).
- ¹⁸P. D. Battle, T. C. Gibb, and P. Lightfoot, *J. Solid State Chem.* **84**, 271 (1990).
- ¹⁹J. Matsuno, T. Mizokawa, A. Fujimori, Y. Takeda, S. Kawasaki, and M. Takano, *Phys. Rev. B* **66**, 193103 (2002).
- ²⁰J. B. Goodenough, in *Progress in Solid State Chemistry*, edited by H. Reiss (Pergamon, London, 1971), Vol. 5.
- ²¹R. J. McQueeney, J. Ma, S. Chang, J.-Q. Yan, M. Hehlen, and F. Trouw, *Phys. Rev. Lett.* **98**, 126402 (2007).
- ²²F. Gao, P. L. Li, Y. Y. Weng, S. Dong, L. F. Wang, L. Y. Lv, K. F. Wang, J.-M. Liu, and Z. F. Ren, *Appl. Phys. Lett.* **91**, 072504 (2007).
- ²³S. Sabyasachi, M. Patra, S. Majumdar, S. Giri, S. Das, V. S. Amaral, O. Iglesias, W. Borghols, and T. Chatterji, *Phys. Rev. B* **86**, 104416 (2012).
- ²⁴L. Lutterotti, S. Matthies, and H. R. Wenk, “MAUD (Material Analysis Using Diffraction) a user friendly Java program for Rietveld texture analysis and more,” in *Proceeding of the Twelfth International Conference on Textures of Materials (ICOTOM-12)* (1999), Vol. 1, p. 1599.
- ²⁵H. R. Wenk, S. Matthies, and L. Lutterotti, *Mater. Sci. Forum* **157–162**, 473 (1994).
- ²⁶M. Ferrari and L. Lutterotti, *J. Appl. Phys.* **76**, 7246 (1994).
- ²⁷X. S. Wu, Y. B. Zuo, J. H. Li, C. S. Chen, and W. Liu, *J. Alloys Compd.* **462**, 432 (2008).
- ²⁸P. D. Battle, T. C. Gibb, and S. Nixon, *J. Solid State Chem.* **79**, 75 (1989).
- ²⁹J. S. Kouvel, *J. Phys. Chem. Solids* **24**, 795 (1963).

- ³⁰C. Tsang, N. Heiman, and K. Lee, *J. Appl. Phys.* **52**, 2471 (1981).
- ³¹J. M. Soares, V. B. Galdino, and F. L. A. Machado, *J. Magn. Magn. Mater.* **350**, 69–72 (2014).
- ³²C. Hohenberg and B. I. Halperin, *Rev. Mod. Phys.* **49**, 435 (1977).
- ³³*Spin Glasses and Random Fields*, Series on Directions in Condensed Matter Physics Vol. 12, edited by A. P. Young (World Scientific, Singapore, 1998).
- ³⁴D. N. H. Nam, K. Jonason, P. Nordblad, N. V. Khiem, and N. X. Phuc, *Phys. Rev. B* **59**, 4189 (1999).
- ³⁵J. Souletie and J. L. Tholence, *Phys. Rev. B* **32**, 516 (1985).
- ³⁶X. N. Ying, *Appl. Phys. Lett.* **101**, 211906 (2012).
- ³⁷A. D. Al-Rawwas, C. E. Johnson, and M. F. Thomas, *Hyperfine Interact.* **93**, 1521 (1994).
- ³⁸W. H. Meiklejohn and C. P. Bean, *Phys. Rev.* **102**, 1413 (1956).
- ³⁹A. E. Berkowitz and K. Takano, *J. Magn. Magn. Mater.* **200**, 552–570 (1999).
- ⁴⁰S. A. McEnroe, B. Carter-Stiglitz, R. H. Harrison, P. Robinson, K. Fabian, and C. McCammon, *Nat. Nanotechnol.* **2**, 631 (2007).